

Topological and holonomic quantum computation based on second-order topological superconductors

Song-Bo Zhang,^{1,*} W. B. Rui,^{2,†} Alessio Calzona,¹ Sang-Jun Choi,¹ Andreas P. Schnyder,² and Björn Trauzettel^{1,3}

¹*Institute for Theoretical Physics and Astrophysics, University of Würzburg, D-97074 Würzburg, Germany*

²*Max-Planck-Institute for Solid State Research, Heisenbergstrasse 1, D-70569 Stuttgart, Germany*

³*Würzburg-Dresden Cluster of Excellence ct.qmat, Germany*

(Dated: December 7, 2021)

Majorana fermions feature non-Abelian exchange statistics and promise fascinating applications in topological quantum computation. Recently, second-order topological superconductors (SOTs) have been discovered to host Majorana fermions as localized quasiparticles with zero excitation energy, pointing out a new avenue to facilitate topological quantum computation. We provide a minimal model for SOTs and systematically analyze the features of Majorana zero modes with analytical and numerical methods. We further construct the fundamental fusion principles of zero modes stemming from a single or multiple SOTS islands. Finally, we propose concrete schemes in different setups formed by SOTs, enabling us to exchange and fuse the zero modes for non-Abelian braiding and holonomic quantum gate operations. We therefore show that universal quantum computing is possible in hardware formed by SOTs.

I. INTRODUCTION

Majorana fermions are self-conjugate fermions¹. They can arise as zero-energy Bogoliubov quasiparticles in condensed matter^{2–5}, such as vortex bound states in p -wave superconductors^{6,7}, Majorana bound states in Josephson junctions^{8,9}, and end states of nanowires with Rashba spin-orbit coupling or of ferromagnetic atomic chains^{10–15}. These bound states have zero excitation energy and are commonly coined Majorana zero modes (MZMs). MZMs are essentially one half of ordinary complex fermions and always come in pairs. When more than two MZMs are present, the braiding (exchange) operations on them correspond to non-Abelian rotations in the ground-state manifold spanned by them. They can thus serve as basic building blocks for topological quantum computation^{3,7,16–18}. If fusions between MZMs are adiabatically tunable, then they could also be exploited for holonomic quantum gates^{19,20}. Hence, how to nucleate, fuse and braid MZMs in solid-state systems is one of the main focuses in modern condensed matter physics and quantum computer science.

Recently, second-order topological superconductors (SOTs) have been discovered in various candidate systems and predicted to host localized MZMs in two dimensions lower than the gapped bulk^{21–43}. This opens up a new avenue towards Majorana-mediated topological quantum computation. Preliminary attempts have been made in this direction^{43–45}, which are, however, limited to only two MZMs. A comprehensive study of creating, fusing and braiding MZMs in SOTs is still lacking. Importantly, the fusion and braiding of more than two MZMs are essential for a successful implementation of (topological) quantum gates^{17,46}.

In this article, we show for the first time that the desired non-Abelian braiding operations of MZMs as well as a full set of holonomic gates can be achieved in the SOTS platform. To elucidate this, we provide a minimal

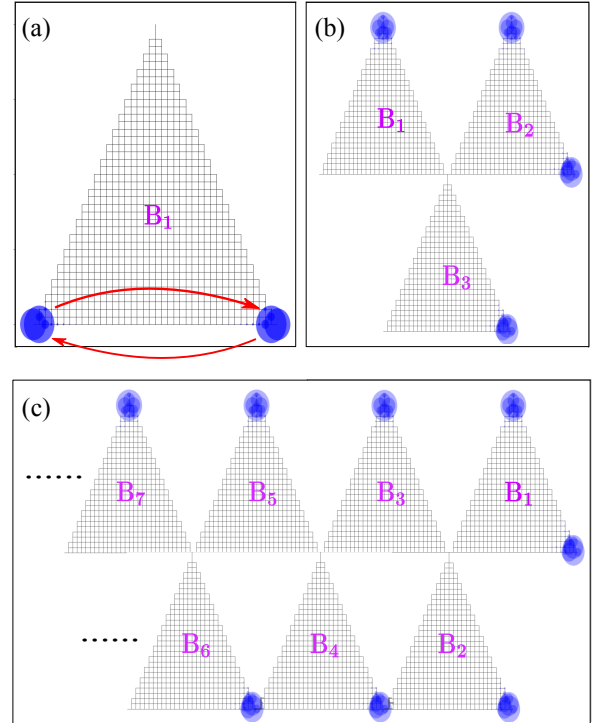


Figure 1. Schematics of the SOTS-based setups for braiding (a) two, (b) four, and (c) more MZMs. The setups are scalable in a straightforward way. \mathbf{B}_i with $i = 1, 2, \dots$ are in-plane magnetic fields applied to the triangle islands. The blue dots indicate the positions of the MZMs.

model for SOTs and discuss the features and behaviors of individual MZMs in a disk geometry, both analytically and numerically. We find that a finite chemical potential breaks an effective mirror symmetry and thus gives rise to tunable spin polarizations of the MZMs. Interestingly, the positions of the MZMs can be controlled by chemical potential and applied in-plane magnetic field.

We systematically analyze the tunneling interaction between adjacent MZMs stemming from a single or multiple SOTS islands and identify the fundamental fusion principles between them. As an illustration of these principles, we demonstrate how to manipulate the fusion of MZMs in an incomplete disk by tuning magnetic field and chemical potential.

We put forward a number of striking setups formed by SOTSs, as sketched in Fig. 1, and present in detail corresponding schemes for braiding the MZMs based on variations of chemical potential, applied magnetic field, and geometry engineering. In a simple triangle setup, we can exchange two MZMs located at the vertices by rotating the magnetic field. In a trijunction setup constructed by three triangle islands, we are able to exchange any two of four MZMs by alternately rotating the magnetic fields applied to the islands. We could extend our theory to a ladder structure which is formed by elementary triangle islands and hosts any number of MZM pairs for braiding performance, see Fig. 1(c). Hence, our proposal is scalable in a straightforward way. Moreover, we propose a shamrock-like trijunction setup constituted by three incomplete disks. This trijunction hosts three MZMs that fuse exclusively with a fourth one. The fusion strengths are smoothly adjustable providing a feasible platform for holonomic quantum gates. Our schemes could be tested in a variety of candidate systems, e.g., quantum spin Hall insulators (QSHIs) in proximity to conventional superconductors and monolayer $\text{FeTe}_{1-x}\text{Se}_x$. Furthermore, they reveal the innovative idea of geometry engineering to braid and fuse MZMs based on SOTSs.

The article is organized as follows. In Sec. II, we introduce the minimal model for SOTSs, derive an effective boundary Hamiltonian and the wavefunctions and spin polarizations of MZMs. Next, we analyze the fusion properties of the MZMs in Sec. III. We proceed to describe the setups and schemes for braiding two or more MZMs, and discuss the important relevant physics in Sec. IV. We devote Sec. V to our proposal of holonomic gates. Finally, we discuss the experimental implementation and measurement, and summarize the results in Sec. VI.

II. MODEL HAMILTONIANS AND MAJORANA ZERO MODES

A. Effective boundary Hamiltonian

We start with considering simple two-dimensional SOTSs which is achieved in QSHIs in presence of superconductivity and moderate in-plane magnetic fields^{40–43}. The minimal model for the SOTSs can be written as $\mathcal{H} = \mathcal{H}_0 + \mathcal{H}_{\text{ex}}$ with

$$\begin{aligned} \mathcal{H}_0 &= m(\mathbf{k})\tau_z\sigma_z + v\sin k_x s_z\sigma_x + v\sin k_y\tau_z\sigma_y - \mu\tau_z, \\ \mathcal{H}_{\text{ex}} &= \Delta(\mathbf{k})\tau_y s_y + g\mu_B B(\cos\theta s_x + \sin\theta s_y\sigma_z), \end{aligned} \quad (1)$$

where $m(\mathbf{k}) = m_0 - 2m(2 - \cos k_x - \cos k_y)$. Without loss of generality, we assume positive parameters v, m

and m_0 , and set the lattice constant a to unity. \mathbf{s} , $\boldsymbol{\sigma}$ and $\boldsymbol{\tau}$ are Pauli matrices acting on spin, orbital, and Nambu spaces, respectively. μ is the chemical potential. The pairing interaction can be s -wave or s_{\pm} -wave. However, the exact form of $\Delta(\mathbf{k})$ is not important for our main results. We take it as a constant $\Delta(\mathbf{k}) = \Delta_0 > 0$ for simplicity. $\mathbf{B} \equiv B(\cos\theta, \sin\theta)$ is the magnetic field with strength B and direction θ . The effective g-factors of the two orbitals are the same in the x direction and opposite in the y direction. This model could effectively describe QSHIs, e.g., an inverted HgTe quantum well^{47,48} with proximity-induced superconductivity, or a monolayer $\text{FeTe}_{1-x}\text{Se}_x$ ^{42,49} under in-plane magnetic fields.

The bulk model (1), in general, has only one crystalline symmetry, inversion symmetry. The existence of MZMs is not restricted to any specific geometry⁵⁰. Moreover, the MZMs appear as low-energy quasiparticles at open boundaries. Thus, to explore the MZMs, we start from the $k \cdot p$ limit of the model (1) and consider the SOTS in a large disk geometry. In the absence of \mathbf{B} , this low-energy model respects an emergent in-plane rotational symmetry. We first derive the boundary states of \mathcal{H}_0 which is decoupled into four blocks representing Dirac Hamiltonians. In the disk, the angular momentum ν is a good quantum number. It is thus convenient to work in polar coordinates: $r = \sqrt{x^2 + y^2}$ and $\varphi = \arctan(y/x)$. The application of \mathbf{B} will break this symmetry. However, in a large disk (with radius $R \gg m/v$), we can approximate a small segment of boundary at an arbitrary angle φ as a straight line. Define an effective coordinate $s \equiv R\varphi$ along the segment and treat the corresponding momentum $p_\nu \equiv \nu/R$ as a quasi-good quantum number. Then, the energy bands of the boundary states of the four blocks can be derived as

$$\begin{aligned} E_{e,\uparrow/\downarrow}(p_\nu) &= \mp v p_\nu - \mu, \\ E_{h,\uparrow/\downarrow}(p_\nu) &= \mp v p_\nu + \mu, \end{aligned} \quad (2)$$

respectively. The boundary states are helical with velocity v . Correspondingly, the wavefunctions can be written as

$$\Psi_{e,\uparrow,p_\nu} = e^{ip_\nu s} K(r)(1, -ie^{i\varphi}, 0, 0, 0, 0, 0)^T, \quad (3)$$

$\Psi_{e,\downarrow,p_\nu} = is_y \Psi_{e,\uparrow,-p_\nu}^*$ and $\Psi_{h,\uparrow/\downarrow,p_\nu} = \tau_x \Psi_{e,\uparrow/\downarrow,-p_\nu}^*$, where $K(r) = \mathcal{N}e^{ip_\nu s}[e^{\lambda_1(r-R)} - e^{\lambda_2(r-R)}]$, $\lambda_{1/2} = v/2m \pm [(v/2m)^2 - m_0/m + p_\nu^2]^{1/2}$ and \mathcal{N} is the normalization factor. We provide more details of this derivation in the Supplemental Materials⁵¹.

With $(\Psi_{e,\uparrow,p_\nu}, \Psi_{e,\downarrow,p_\nu}, \Psi_{h,\uparrow,p_\nu}, \Psi_{h,\downarrow,p_\nu})$ as the basis, we next project the full Hamiltonian onto the boundary states. The resulting effective Hamiltonian on the boundary can be written as

$$\tilde{\mathcal{H}} = \begin{pmatrix} -vp_\nu - \mu & ie^{-i\varphi}\tilde{B} & 0 & -\Delta_0 \\ -ie^{i\varphi}\tilde{B} & vp_\nu - \mu & \Delta_0 & 0 \\ 0 & \Delta_0 & -vp_\nu + \mu & ie^{i\varphi}\tilde{B} \\ -\Delta_0 & 0 & -ie^{-i\varphi}\tilde{B} & vp_\nu + \mu \end{pmatrix}, \quad (4)$$

where $\tilde{B} = B \sin(\varphi - \theta)$ and $g\mu_B = 1$ has been chosen for convenience. The effective pairing potential Δ_0 felt by the boundary states is constant and independent of the boundary orientation. It couples electrons to holes with opposite spins and preserves time-reversal and in-plane rotational symmetries. Thus, the energy spectrum is fully gapped in the absence of B . This implies that the pairing interaction alone cannot lead to a second-order topological phenomenon. The scenario becomes different when we turn on B . The magnetic field couples states with opposite spins and breaks the rotational symmetry. The effective magnetic field \tilde{B} depends substantially on the angular position φ (or equivalently, the boundary orientation which is parallel to the azimuthal direction at φ). Consequently, interesting physics including controllable MZMs arise, which we discuss in detail below.

B. MZMs and their positions

When $\mu = 0$, through a unitary transformation $U(\varphi) = e^{-i\pi\tau_x/4} e^{i\varphi\tau_z s_z/2}$, where \mathbf{s} and $\boldsymbol{\tau}$ are Pauli matrices acting on spin and Nambu spaces of boundary states, respectively, Eq. (4) can be brought into block-diagonal form

$$U(\varphi)\tilde{\mathcal{H}}(\varphi)U^{-1}(\varphi) = h_u \oplus h_d, \quad (5)$$

where $h_{u/d} = -vp_\nu s_z + (\tilde{B} \pm \Delta_0)s_y$. The two blocks $h_{u/d}$ are essentially one-dimensional Dirac Hamiltonians with the masses given by $\tilde{B} \pm \Delta_0$, respectively. They can be connected not only by inversion \mathcal{P} but also by an effective mirror symmetry \mathcal{M} with the mirror line in the field direction. Note that \mathcal{P} and \mathcal{M} act nonlocally on the boundary model, i.e., $\tilde{\mathcal{P}}\tilde{\mathcal{H}}(p_\nu, \varphi)\tilde{\mathcal{P}}^{-1} = \tilde{\mathcal{H}}(p_\nu, \varphi + \pi)$ and $\tilde{\mathcal{M}}\tilde{\mathcal{H}}(p_\nu, \varphi - \theta)\tilde{\mathcal{M}}^{-1} = \tilde{\mathcal{H}}(-p_\nu, \theta - \varphi)$, where the overhead tilde (\sim) indicates boundary-state space. For h_d , the inclusion of $B > \Delta_0$ changes the sign of the Dirac mass at $\varphi_1 = \theta + \arcsin(\Delta_0/B)$ and $\varphi_2 = \theta - \arcsin(\Delta_0/B) + \pi$. Thus, two localized Majorana states with zero energy appear, which we label as γ_1 and γ_2 . If inversion symmetry is present, then another pair of MZMs, labeled as γ_3 and γ_4 , can be found from h_u . They are located at the positions different from φ_1 and φ_2 by an angle π .

When $\mu \neq 0$, the transformed Hamiltonian (5) is no longer block diagonal. Nevertheless, the four bands of the Hamiltonian can still be analytically derived:

$$E = \pm \sqrt{\tilde{B}^2 + A^2 p_\nu^2 + \bar{\Delta}^2 \pm 2\sqrt{\tilde{B}^2 \bar{\Delta}^2 + A^2 \mu^2 p_\nu^2}}, \quad (6)$$

where $\bar{\Delta} = \sqrt{\Delta_0^2 + \mu^2}$. Increasing $|\tilde{B}|$ from 0 to a value larger than $\bar{\Delta}$, we observe band inversions happening at $p_\nu = 0$. Suppose that B is sufficiently large, $B^2 > \bar{\Delta}^2$, then, due to the oscillatory behavior of \tilde{B} , the band order changes when moving along the disk boundary. This indicates the appearance of MZMs. The positions of the MZMs are determined by the closing points of the bands.

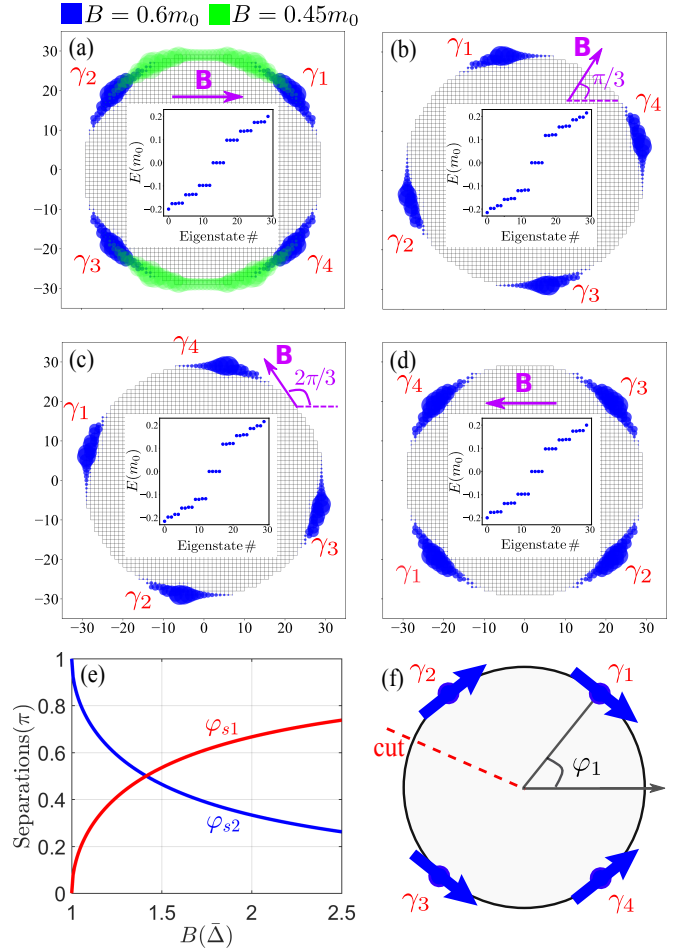


Figure 2. Majorana zero modes in a disk geometry. (a)-(d) The blue color indicates the positions of the MZMs for magnetic fields in different directions, (a) $\theta = 0$, (b) $\pi/3$, (c) $2\pi/3$ and (d) π , respectively. By rotating the magnetic field \mathbf{B} , the MZMs circle around the disk boundary. Inserts are the corresponding energy spectra. Four MZMs are protected by an energy gap from excited modes. The positions of the MZMs depend also on the strength of magnetic field B and chemical potential μ . (e) Separations φ_{s1} and φ_{s2} as functions of B (in units of $\bar{\Delta}$). (f) Schematic of the spin polarizations of the MZMs at a finite chemical potential μ . Here, we choose the following representative parameter values: $\mu = 0.05m_0$, $\Delta_0 = 0.4m_0$, $B = 0.6m_0$, $v = m = m_0 = 1$ and $N_r = 30$. For the green color in (a), we use $B = 0.45m_0$.

Thus, the positions φ_i of MZMs γ_i (with $i \in \{1, 2, 3, 4\}$) are generally given by

$$\begin{aligned} \varphi_{1/4} &= \theta \pm \arcsin(\bar{\Delta}/B), \\ \varphi_{2/3} &= \theta \mp \arcsin(\bar{\Delta}/B) + \pi, \end{aligned} \quad (7)$$

where $0 \leq \varphi_1 - \theta < \pi/2$. Similar to the MZMs in the $\mu = 0$ limit, γ_1 (γ_2) and γ_3 (γ_4) are always separated by an angle π . They are related to each other by inversion symmetry. In contrast, the separations between the neighboring MZMs γ_1 (γ_2) and γ_4 (γ_3) and γ_1 (γ_3) and

	γ_1	γ_2	γ_3	γ_4
Position φ_i	$\theta + \arcsin(\bar{\Delta}/B)$	$\theta - \arcsin(\bar{\Delta}/B) + \pi$	$\theta + \arcsin(\bar{\Delta}/B) + \pi$	$\theta - \arcsin(\bar{\Delta}/B)$
Wavefunction Ψ_i	$\mathcal{F}_+ \begin{pmatrix} e^{-i(\varphi_1 - \vartheta + \pi/2)/2} \\ -e^{i(\varphi_1 + \vartheta + \pi/2)/2} \\ e^{i(\varphi_1 - \vartheta - \pi/2)/2} \\ e^{-i(\varphi_1 + \vartheta - \pi/2)/2} \\ e^{i(\varphi_1 - \vartheta + \pi/2)/2} \\ -e^{-i(\varphi_1 + \vartheta + \pi/2)/2} \\ e^{-i(\varphi_1 - \vartheta - \pi/2)/2} \\ e^{i(\varphi_1 + \vartheta - \pi/2)/2} \end{pmatrix}$	$\mathcal{F}_- \begin{pmatrix} -e^{-i(\varphi_2 + \vartheta + \pi/2)/2} \\ e^{i(\varphi_2 - \vartheta + \pi/2)/2} \\ e^{i(\varphi_2 + \vartheta - \pi/2)/2} \\ e^{-i(\varphi_2 - \vartheta - \pi/2)/2} \\ -e^{i(\varphi_2 + \vartheta + \pi/2)/2} \\ e^{-i(\varphi_2 - \vartheta + \pi/2)/2} \\ e^{-i(\varphi_2 + \vartheta - \pi/2)/2} \\ e^{i(\varphi_2 - \vartheta - \pi/2)/2} \end{pmatrix}$	$\mathcal{F}_+ \begin{pmatrix} e^{-i(\varphi_3 - \vartheta - \pi/2)/2} \\ e^{i(\varphi_3 + \vartheta - \pi/2)/2} \\ -e^{i(\varphi_3 - \vartheta + \pi/2)/2} \\ e^{-i(\varphi_3 + \vartheta + \pi/2)/2} \\ e^{i(\varphi_3 - \vartheta - \pi/2)/2} \\ e^{-i(\varphi_3 + \vartheta - \pi/2)/2} \\ -e^{-i(\varphi_3 - \vartheta + \pi/2)/2} \\ e^{i(\varphi_3 + \vartheta + \pi/2)/2} \end{pmatrix}$	$\mathcal{F}_- \begin{pmatrix} e^{-i(\varphi_4 + \vartheta - \pi/2)/2} \\ e^{i(\varphi_4 - \vartheta - \pi/2)/2} \\ e^{i(\varphi_4 + \vartheta + \pi/2)/2} \\ -e^{-i(\varphi_4 - \vartheta + \pi/2)/2} \\ e^{-i(\varphi_4 + \vartheta - \pi/2)/2} \\ e^{-i(\varphi_4 - \vartheta - \pi/2)/2} \\ e^{-i(\varphi_4 + \vartheta + \pi/2)/2} \\ -e^{i(\varphi_4 - \vartheta + \pi/2)/2} \end{pmatrix}$
Polarization $\mathbf{S}^{(e/h)}$	$\pm S_0(\sin \varphi_1, -\cos \varphi_1, 0)$	$\pm S_0(\sin \varphi_2, -\cos \varphi_2, 0)$	$\pm S_0(-\sin \varphi_3, \cos \varphi_3, 0)$	$\pm S_0(-\sin \varphi_4, \cos \varphi_4, 0)$

Table I. Wavefunctions and spin polarizations of MZMs in an SOTS island. The basis for the wavefunctions is the same as the one of the model (1). The factors \mathcal{F}_\pm account for the spatial distribution and normalization of the wavefunctions. The magnitude of the spin polarizations $\mathbf{S}^{(e/h)} \equiv (S_x^{(e/h)}, S_y^{(e/h)}, S_z^{(e/h)})$ is given by $S_0 = \hbar\mu/(4\bar{\Delta})$. The subscripts (e/h) stand for the electron and hole parts, respectively. The spin polarizations of the electron and hole parts are opposite, $\mathbf{S}_{\gamma_i}^{(h)} = -\mathbf{S}_{\gamma_i}^{(e)}$, as required by the Majorana nature of γ_i .

γ_2 (γ_4) are respectively given by

$$\varphi_{s1} = 2 \arcsin(\bar{\Delta}/B), \text{ and } \varphi_{s2} = \pi - \varphi_{s1}. \quad (8)$$

These separations are independent of the field direction θ . However, they are controllable by chemical potential μ and field strength B , via the ratio $\bar{\Delta}/B$. Increasing B or decreasing μ , φ_{s1} is monotonically increased whereas φ_{s2} is decreased, as shown in Fig. 2(e).

Interestingly, the positions of γ_i depend not only on the ratio $\bar{\Delta}/B$ but also on the field direction, according to Eq. (7). When rotating \mathbf{B} , the MZMs γ_i move around the disk boundary. To confirm these features, we employ the tight-binding model (1) and define the disk by $i_x^2 + i_y^2 \leq N_r^2$, where N_r is the radius of the disk and i_x, i_y label the lattice sites in the x and y directions, respectively. We use the Kwant package⁵² to plot the wavefunctions. For a large magnetic field $B > \bar{\Delta}$ applied in the x direction, we clearly identify four MZMs centered at the symmetric positions obeying $\varphi_1 = -\varphi_4$ and $\varphi_{2/3} = \varphi_{4/1} + \pi$, see Fig. 2(a). When rotating \mathbf{B} from x to $-x$ direction, all the MZMs are moving anticlockwise. However, their separations are unchanged, see Fig. 2(a)–(d). These observations perfectly agree with our analytical results. Moreover, we find that although the positions of the MZMs are quite different for different θ , the energy spectra of the disks are almost the same. There is always an energy gap protecting the MZMs from excited modes, as long as the MZMs are well separated.

C. Wavefunctions and spin polarizations of MZMs

With the help of the boundary Hamiltonian (4), the wavefunctions of the MZMs γ_i (with $i \in \{1, 2, 3, 4\}$) can be analytically derived. We summarize the results in Table I and provide the detailed derivations in the Supplemental Material⁵¹. In the table, the factors $\mathcal{F}_\pm =$

$\mathcal{N}e^{\pm \int^s \xi(s') ds'}$ with $\xi = \Delta_0 - (\tilde{B}^2 - \mu^2)^{1/2}$ account for the spatial distribution and normalization of the wavefunctions Ψ_i . These factors indicate that the wavefunctions decay exponentially away from the corresponding centers φ_i . From Table I, several important remarks can be deduced. First of all, the wavefunctions are self-adjoint: $\Psi_i = \tau_x \Psi_i^*$, which verifies the basic Majorana property of γ_i . Recall that γ_1 (γ_2) and γ_3 (γ_4) are separated by an angle π . We can find that $\Psi_3 = -\mathcal{P}\Psi_1$ and $\Psi_4 = \mathcal{P}\Psi_2$, where $\mathcal{P} = \sigma_z \mathcal{T}_{\varphi \rightarrow \varphi + \pi}$ is the inversion symmetry operator and $\mathcal{T}_{\varphi \rightarrow \varphi + \pi} = e^{-i\pi \tau_z s_z \sigma_z / 2}$ shifts the angle φ by π . These relations reflect the fact that γ_1 (γ_2) is transformed to γ_3 (γ_4) by inversion symmetry, as mentioned before. It is also important to note that the wavefunctions obey antiperiodic boundary conditions, $\Psi_i(\varphi) = -\Psi_i(\varphi + 2\pi)$. This implies that when moving around the boundary, the MZMs effectively traverse a branch cut where they change sign, as sketched by the red dashed line in Fig. 2(f). The sign change across the cut is instructive to better understand the braiding of MZMs⁷, as discussed below.

Let us now look at the spin polarizations of the MZMs. When $\mu = 0$, the disk system respects the effective mirror symmetry, as mentioned before. Then, the MZMs are spinless. However, in the presence of $\mu \neq 0$, the mirror symmetry is no longer preserved. Hence, the MZMs acquire finite spin polarizations in the x - y plane, see Table I. The polarization magnitudes are given by $\hbar\mu/(4\bar{\Delta})$. In the limit $|\mu| \gg \Delta_0$, the MZMs become fully polarized. The polarization directions depend on φ_i . They always point parallel or anti-parallel to the boundary orientation, as illustrated in Fig. 2(f). Thus, when moving the MZMs, their spin polarizations rotate. Since γ_1 and γ_3 are separated by π , they have the same polarization. Similarly, γ_2 and γ_4 have also an identical polarization. Note that the spin polarizations of γ_i could be detected by magnetic tunneling experiments.

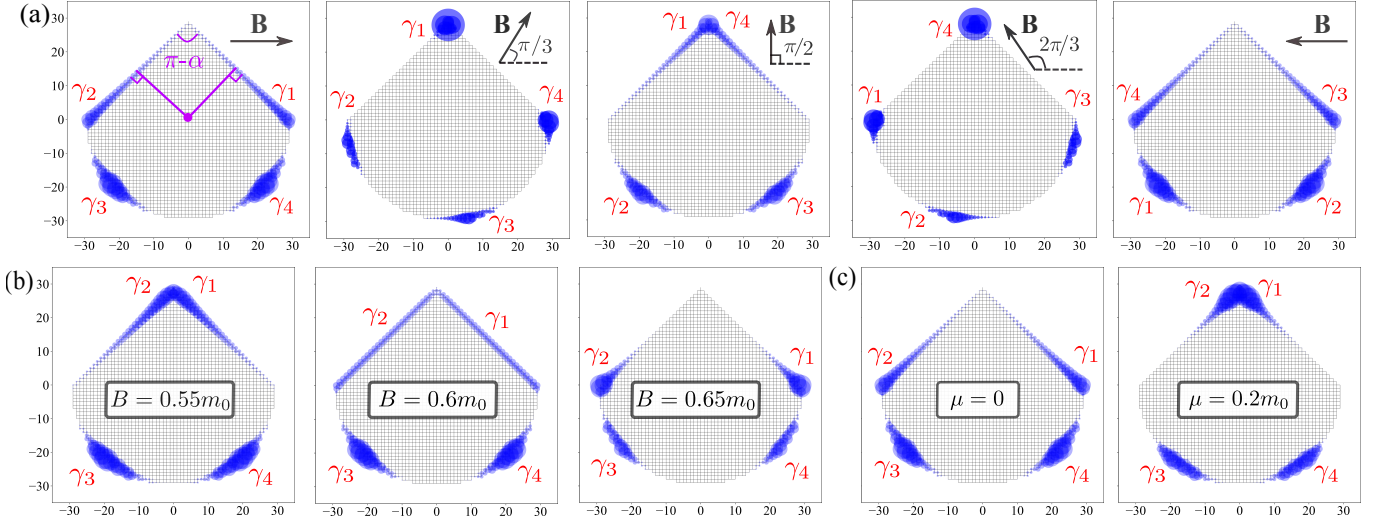


Figure 3. Manipulation of the fusion of MZMs in an incomplete disk. (a) Controlling the fusion by tuning θ . At the field direction $\theta = \theta_c \in \{0, \pi/4, \pi/2, 3\pi/4\}$ modulo π , two adjacent MZMs collide into the sharp vertex and fuse. Tuning θ away from θ_c splits the two MZMs from the vertex and weakens their fusion. (b) Controlling the fusion by tuning B . The MZMs γ_1 and γ_2 are well separated for $B > B_{c1}$, whereas they collide and fuse (at the vertex) for $B < B_{c1}$, where $B_{c1} = \bar{\Delta}/\sin(\alpha/2)$. (c) Controlling the fusion by tuning μ . γ_1 and γ_2 are separated for $|\mu| < \mu_{c1}$ with $\mu_{c1} = [B^2 \sin^2(\alpha/2) - \bar{\Delta}_0^2]^{1/2}$, whereas they collide and fuse for $|\mu| > \mu_{c1}$. $\mu = 0.05m_0$ in (a) and 0 in (b), $B = 0.6m_0$ and $\theta = 0$ in (a,c), and, for all panels, all other parameters are the same as those in Fig. 2

III. FUSION BETWEEN MZMS

We proceed to discuss the fusion between the MZMs. Let us first consider the disk geometry with vanishing μ . Two adjacent MZMs can be brought close to each other by tuning μ or B , according to Eq. (8). If the two MZMs belong to the same block of Eq. (5), e.g., γ_1 and γ_2 (or γ_3 and γ_4), then they fuse with each other and acquire a hybridization energy which depends exponentially on their distance in space. In contrast, since h_u and h_d do not interact with each other due to the effective mirror symmetry, $\gamma_{1/2}$ stemming from h_u cannot fuse with $\gamma_{3/4}$ which stem from the other block h_d , even if they sit at the same position and have strong overlap in wavefunction.

A finite μ , however, couples the two blocks. Therefore, the fusion between $\gamma_{1/4}$ ($\gamma_{2/3}$) is allowed. In the SOTSs, the fusion of MZMs is realized by the hopping interaction which depends on the momentum-orbital coupling. According to Eq. (1), the corresponding operators in the x and y directions can be found as $\hat{T}_x = ivs_z\sigma_x/2 + m\tau_z\sigma_z$ and $\hat{T}_y = iv\tau_z\sigma_y/2 + m\tau_z\sigma_z$, respectively. Thus, the fusion (also called coupling) strength between two MZMs, say γ_i and γ_j (with $i, j \in \{1, 2, 3, 4\}$), can be calculated as $|\langle\Psi_i|(\hat{T}_x + \hat{T}_y)|\Psi_j\rangle|$. We summarize the results in Table II. In a homogeneous system, the fusion between $\gamma_{1/2}$ ($\gamma_{3/4}$) is proportional to $\cos\vartheta$, while the one between $\gamma_{1/4}$ ($\gamma_{2/3}$) is linear in $\sin\vartheta$, where $\vartheta = \arctan(\mu/\Delta_0)$. The proportionality is determined by the overlap of the wavefunctions of the two involved MZMs. In contrast, in a single SOTS island, γ_1 and γ_3 (γ_2 and γ_4) are well separated in space. Moreover, they are related by inversion

symmetry. Notice that \hat{T}_x and \hat{T}_y anti-commute with the inversion operator \mathcal{P} . The fusion between $\gamma_{1/3}$ ($\gamma_{2/4}$) is prohibited even in the presence of finite μ . These results are generic and also apply to the case where the two MZMs belong to different connected SOTS islands with the same pairing phase. However, if two islands have a pairing phase difference $2\Phi \neq 2n\pi$ with $n \in \{0, \pm 1, \dots\}$, then γ_1 (γ_2) stemming from one island can also fuse with γ_3 (γ_4) from the other island, see Table II. The fusion induced by a phase difference can be exploited to realize the braiding of more than two MZMs, which we demonstrate below.

In a full disk, all angular positions φ are available. Thus, the four MZMs related by inversion symmetry ap-

	γ_1	γ_2	γ_3	γ_4
γ'_1	\times	$\cos\vartheta \cos\Phi$	$\sin\Phi$	$\sin\vartheta \cos\Phi$
γ'_2	$\cos\vartheta \cos\Phi$	\times	$\sin\vartheta \cos\Phi$	$\sin\Phi$
γ'_3	$\sin\Phi$	$\sin\vartheta \cos\Phi$	\times	$\cos\vartheta \cos\Phi$
γ'_4	$\sin\vartheta \cos\Phi$	$\sin\Phi$	$\cos\vartheta \cos\Phi$	\times

Table II. Fusion of adjacent MZMs located in the same or different connected SOTS islands. The pairing phase difference between the two islands is 2Φ . For simplicity, we assume the same μ in all islands. The factors that depend on the wavefunction overlap are not displayed. \times means that the fusion is impossible. The results for the case of a single island are obtained by $\gamma'_i = \gamma_i$ and $\Phi = 0$. We provide more details about the table in the Supplemental Material⁵¹.

pear or disappear simultaneously. To better understand the fusion behaviors, it is instructive to consider a geometry that breaks inversion symmetry. For concreteness, we consider in the following an incomplete disk made by cutting off two symmetric pieces normal to two radial directions and with a vertex angle $\pi - \alpha$ between the cutting lines, as illustrated in Fig. 3. This simple setup enables us to manipulate the fusion of adjacent MZMs in different ways.

We are able to control the fusion by tuning the field direction θ , depending on the value of α which measures the range of angles missing in the setup. If $\alpha > \max(\varphi_{s1}, \varphi_{s2})$, then we can move any two adjacent MZMs into the vertex and fuse them by tuning θ , see Fig. 3(a). Take the reflection-symmetry line of the incomplete disk in the x direction for instance. At $\theta = 0, \pi/4, \pi/2$ and $3\pi/4$ (modulo π), respectively, the adjacent pairs of $\gamma_{1/2}$, $\gamma_{4/1}$, $\gamma_{3/4}$, and $\gamma_{2/3}$ are maximally fused. Note that the fusion between $\gamma_{1/4}$ ($\gamma_{2/3}$) always requires a finite μ . If $\min(\varphi_{s1}, \varphi_{s2}) < \alpha < \max(\varphi_{s1}, \varphi_{s2})$, then only the adjacent pairs with angular separation given by $\min(\varphi_{1s}, \varphi_{2s})$ can be fused. Whereas the other adjacent pairs with angular separation $\max(\varphi_{s1}, \varphi_{s2})$ can never be pushed to the vertex together and their fusions are suppressed. Finally, if $\alpha < \min(\varphi_{s1}, \varphi_{s2})$, then we cannot fuse the MZMs at all.

Since the separations φ_{s1} and φ_{s2} depend on the ratio $\bar{\Delta}/B$, we can also modulate the fusion by tuning B or μ . As an illustration, we first tune \mathbf{B} with the field direction set at $\theta = 0$, such that two MZMs, say γ_1 and γ_2 , are brought close to the vertex, see Fig. 3(b). When $B > B_{c1} \equiv \bar{\Delta}/\sin(\alpha/2)$, the separation φ_{1s} between $\gamma_{1/2}$ is larger than α . Thus, γ_1 and γ_2 remain well separated. In contrast, when $B < B_{c1}$, we find $\varphi_{1s} < \alpha$. Then, γ_1 and γ_2 collide and fuse at the vertex. At the critical point $B = B_{c1}$, γ_1 and γ_2 extend along the cutting lines, see the middle panel of Fig. 3(b). In all the cases, the other MZMs remain well separated and stay at zero energy. Similarly, we can set \mathbf{B} to other proper directions, e.g., $\theta = \pi/4, \pi/2$ or $3\pi/4$, and control the fusion of other adjacent pairs by tuning B . For the pair of $\gamma_{1/4}$ (or $\gamma_{2/3}$), the critical field is given by $B_{c2} = \bar{\Delta}/\cos(\alpha/2)$. The fusion is achieved when $B > B_{c2}$. Alternatively, we can fix B and θ and instead use μ to electrically control the fusion. For the pair of $\gamma_{1/2}$ (or $\gamma_{3/4}$), the fusion is enhanced when $|\mu| > \mu_{c1}$ and suppressed when $|\mu| < \mu_{c1}$, where $\mu_{c1} = [B^2 \sin^2(\alpha/2) - \bar{\Delta}_0^2]^{1/2}$, see Fig. 3(c). For the pair of $\gamma_{1/4}$ (or $\gamma_{2/3}$), the critical μ reads $\mu_{c2} = [B^2 \cos^2(\alpha/2) - \bar{\Delta}_0^2]^{1/2}$ and the fusion is reduced when $|\mu| > \mu_{c2}$ whereas revived when $|\mu| < \mu_{c2}$.

IV. BRAIDING MAJORANA ZERO MODES AND NON-ABELIAN STATISTICS

A. Braiding two Majorana zero modes

We have shown that there are four MZMs on the boundary of a disk. By geometry engineering, i.e., line cutting, and making certain angular positions unavailable, we are able to selectively squeeze two MZMs into the same position and fuse them there. In this section, we show that a single triangle setup with a finite μ enables us to fuse two out of the four MZMs, while the other two modes remain at zero energy. Such a setup allows us to exchange the remaining two MZMs by rotating the magnetic field \mathbf{B} , without interference from the other modes. The three angles of the triangle are assumed to be smaller than $\min(\varphi_{s1}, \varphi_{s2})$. We label the remaining MZMs by γ_α and γ_β , respectively, and discuss the exchange process based on numerical simulations below.

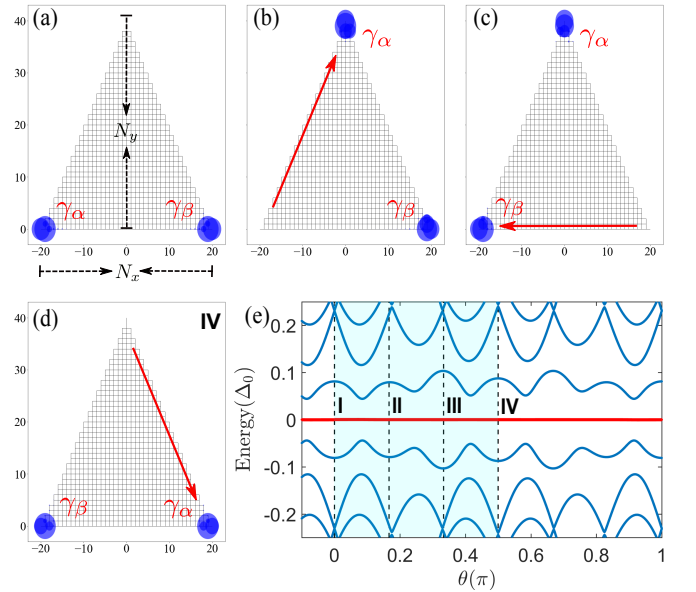


Figure 4. Exchanging two MZMs by varying θ . (a)-(d) Positions of the two MZMs at $\theta = 0, \pi/6, \pi/3$ and $\pi/2$, respectively. (e) Energy spectrum with respect to θ . There are always two zero MZMs, γ_α and γ_β (the red flat bands). (a)-(d) correspond to the moments labeled by **I-IV**, respectively. Turning $\theta = 0 \rightarrow \pi/2$, γ_α and γ_β exchange their positions effectively. We provide an animation for this process in the Supplemental Material⁵¹. The dimensions of the triangle are $N_x = N_y = 40$, $\mu = 0.1m_0$, and all other parameters are the same as those in Fig. 2.

Let us start from the state with \mathbf{B} applied in the x direction, i.e., $\theta = 0$. In the initial state, γ_α sits at the left vertex while γ_β sits at the right vertex, see Fig. 4(a). We adiabatically turn $\theta = 0 \rightarrow \pi/2$. As a consequence, the following movements occur in sequence. First, γ_β smoothly shifts to the top vertex, while γ_α stays at the left vertex, see Fig. 4(b). Then, γ_β stays at the top vertex

while γ_α shifts to the right vertex, where γ_β was sitting in the initial state. Finally, γ_α stays at the right vertex, while γ_β shifts down to the left vertex. We can clearly trace the movements of each MZM⁵¹. Apparently, γ_α and γ_β effectively exchange their positions. It is important to note that, during the entire process, γ_α and γ_β stay robustly at zero energy and they are protected from mixing with other modes by a finite energy gap, as shown by the instantaneous spectrum in Fig. 4(e). It indicates that the degeneracy of the ground states remains unchanged, which is a necessary condition for an adiabatic operation.

We now analyze the initial and final quantum states formed by γ_α and γ_β in the triangle island. It is instructive to view the vertices of the triangle on the boundary of a disk. We can then identify the process of braiding with a movement of the two MZMs around this boundary. As a result, one of the MZMs, say γ_α , must pass the cut and change sign due to the antiperiodic boundary conditions. Therefore, the exchange rule of the two MZMs is given by: $\gamma_\alpha \mapsto \gamma_\beta$ and $\gamma_\beta \mapsto -\gamma_\alpha$. The exchange operator in terms of Majorana operators can then be constructed as $\hat{T} = (1 + \gamma_\beta \gamma_\alpha) / \sqrt{2}$.⁷ The two MZMs may define a complex fermion with the operator as $f = (\gamma_\alpha + i\gamma_\beta) / 2$. Thus, there are two ground states, $|0\rangle$ and $|1\rangle \equiv f^\dagger |0\rangle$, which correspond to the absence and presence of the complex fermion, respectively. The exchange operation can be rewritten as $\hat{T}_{\alpha\beta} = \exp[i\pi(f^\dagger f - f f^\dagger)/4]$. It acts diagonally in the ground-state space $\{|0\rangle, |1\rangle\}$, and adds opposite Berry phases $\pm\pi/4$ to the two ground states.

B. Braiding more Majorana zero modes

To exploit the non-Abelian statistics of braiding operations for topological quantum computation, more than two MZMs are required⁴⁶. To this end, we consider a tri-junction made by connecting three triangle islands in the center, as illustrated in Fig. 5. We apply a finite chemical potential but different pairing phases in the three islands. As we have shown before, the triangle islands would each host a couple of MZMs at the vertices if they were not connected. However, as the islands have their vertices connected in the center, two MZMs are fused. Therefore, totally only four MZMs remain in the setup: two in one island and the other two in the other two islands, respectively. We denote the islands as $T1$, $T2$ and $T3$, and the MZMs γ_a , γ_b , γ_c and γ_d , respectively. Assume that three magnetic fields can be independently tuned in the three islands. With these preconditions, we show that this tri-junction allows to braid any two of the four MZMs while keeping the other MZMs untouched. The two MZMs in the same island can be braided by rotating the corresponding magnetic field in the same way as described in the previous section. Thus, we focus on the braiding of two MZMs from different islands in the following.

Let us start by considering the situation where the magnetic fields \mathbf{B}_i are applied uniformly, namely, $B_i = B_0$ and $\theta_i = -\pi/3$ (with $i \in \{1, 2, 3\}$). At this moment,

γ_a is located in $T1$, γ_b and γ_c in $T2$, and γ_d in $T3$, as shown in Fig. 5(a). We braid γ_a and γ_b in three steps in sequence. In the first step, we turn $\theta_2 = -\pi/3 \rightarrow -\pi/2$ and move γ_b slowly to the center. After this step, $T1$ has two MZMs, γ_a and γ_b , see Fig. 5(b). In the second step, we turn $\theta_1 = -\pi/3 \rightarrow \pi/6$. This results in the exchange of γ_a and γ_b inside $T1$, see Fig. 5(b)-(e). In the last step, we rotate θ_2 back to $-\pi/3$. Thus, γ_a is moved smoothly to the top vertex of $T2$. Therefore, the positions of γ_a and γ_b are exchanged. Importantly, during the entire process the four MZMs stay robustly at zero energy and they are also protected from high-energy modes by a finite energy gap, see Fig. 5(g). In a similar way, we can braid γ_c and γ_d by rotating θ_2 and θ_3 alternatively. The three exchanges $\gamma_a \leftrightarrow \gamma_b$, $\gamma_b \leftrightarrow \gamma_c$ and $\gamma_c \leftrightarrow \gamma_d$ generate the whole braid group of the four MZMs.

Next, we discuss the interpretation of braiding γ_a and γ_b in terms of quantum gates à la Ivanov⁷. There are totally four MZMs in the setup. In the initial state, both γ_b and γ_c are in $T2$. We combine γ_b and γ_c to define a complex fermion $f_{bc} = (\gamma_b + i\gamma_c)/2$. Then, we have two degenerate ground states $|0_{bc}\rangle$ and $|1_{bc}\rangle \equiv f_{bc}^\dagger |0_{bc}\rangle$ of $T2$ with different fermion parity. Analogously, we can define another complex fermion as $f_{da} = (\gamma_d + i\gamma_a)/2$. Then, $|0_{da}\rangle$ and $|1_{da}\rangle \equiv f_{da}^\dagger |0_{da}\rangle$ would correspond to two ground states of $T1$ and $T3$ with different total fermion parity. Considering the three islands together, for a fixed global fermion parity, there are only two ground states which span the computational space of a single non-local qubit. Without loss of generality, we assume even fermion parity and write the two ground states as $|\bar{0}\rangle \equiv |0_{bc}, 0_{da}\rangle$ and $|\bar{1}\rangle \equiv |1_{bc}, 1_{da}\rangle$. The exchange operator $T_{ab} = (1 + \gamma_b \gamma_a) / \sqrt{2}$ of γ_a and γ_b can be written as $T_{ab} = (\sigma_0 - i\sigma_x) / \sqrt{2}$ in the basis $\{|\bar{0}\rangle, |\bar{1}\rangle\}$. It corresponds to a $\pi/2$ rotation in the Bloch sphere around the x axis and thus mixes the qubit. The same result is obtained by exchanging γ_c and γ_d . Similarly, the exchange $\gamma_b \leftrightarrow \gamma_c$ (or $\gamma_a \leftrightarrow \gamma_d$) corresponds to a $\pi/2$ rotation around the z axis. Instead, they act diagonally on the qubit. These rotations are clearly non-commutative, consistent with the non-Abelian nature of the MZMs.

The triangle setups and schemes described above can be further generalized to the case with more pairs of MZMs. As a natural generalization, we consider a ladder structure formed by N_{tri} elementary triangle islands T_i with finite chemical potential, as sketched in Fig. 1(c). N_{tri} is assumed to be an odd integer. Three islands connected by the same point have different pairing phases. For example, we may use $\Phi_{3n-2} = 0$ and $\Phi_{3n-1} = -\Phi_{3n} = 2\pi/3$ with $n \in \{1, 2, \dots\}$. For uniform magnetic fields, say, with directions $\theta_i = -\pi/3$, this ladder setup supports $N_{\text{tri}} + 1$ MZMs in total. The setup can be scaled up by adding extra islands. We can braid any two of the MZMs by alternately varying the magnetic fields in an analogous way as described before in the triangle setups. Notably, since the braiding operations are topological, the choice of chemical potential and pairing phases and the controlling of magnetic fields do not need

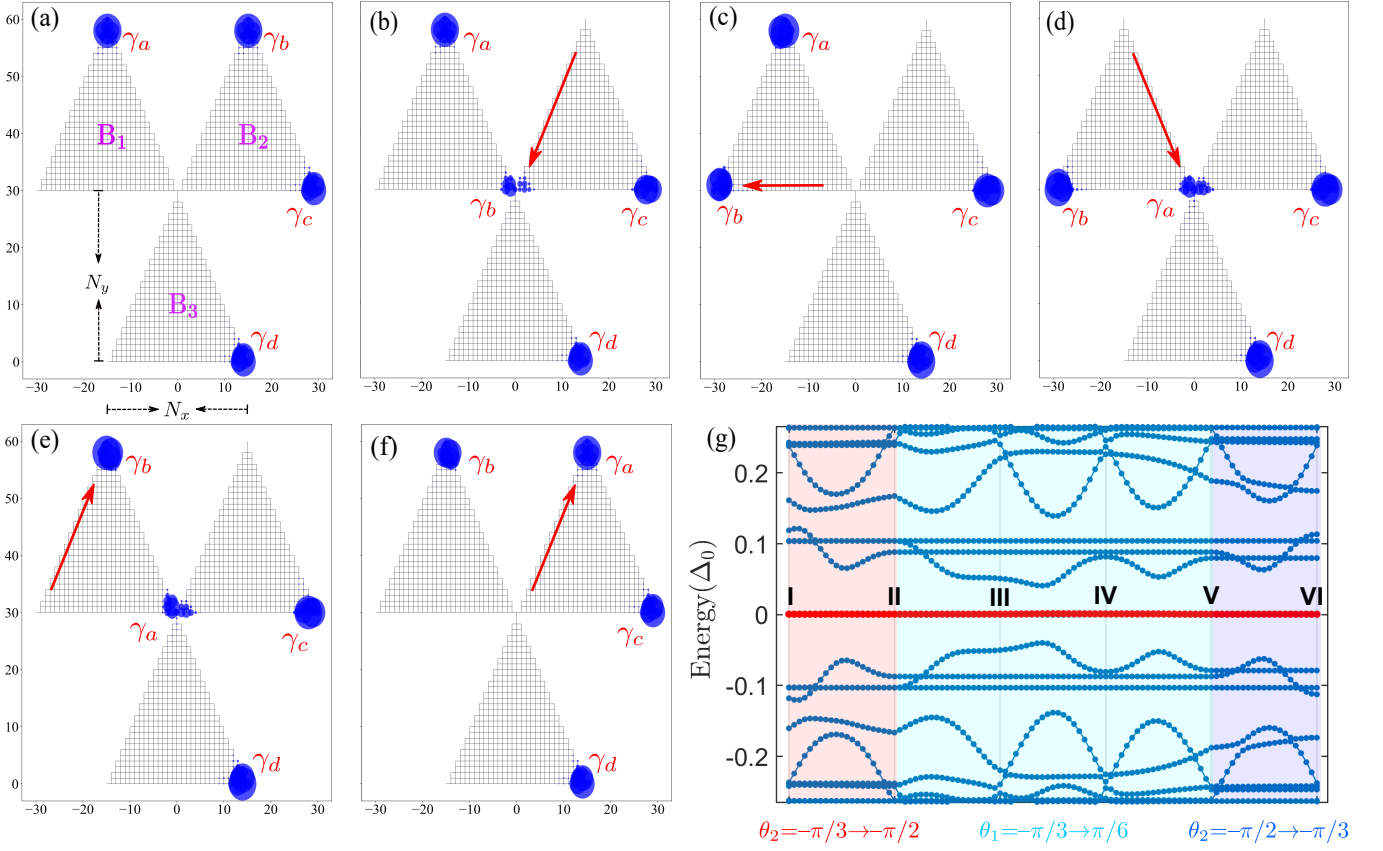


Figure 5. Braiding four MZMs by rotating in-plane magnetic fields. Positions of the four MZMs at (a) $(\theta_1, \theta_2, \theta_3) = -(\pi/3, \pi/3, \pi/3)$, (b) $(\theta_1, \theta_2, \theta_3) = -(\pi/3, \pi/2, \pi/3)$, (c) $(\theta_1, \theta_2, \theta_3) = -(\pi/6, \pi/2, \pi/3)$, (d) $(\theta_1, \theta_2, \theta_3) = -(0, \pi/2, \pi/3)$, (e) $(\theta_1, \theta_2, \theta_3) = (\pi/6, -\pi/2, -\pi/3)$, and (f) $(\theta_1, \theta_2, \theta_3) = (\pi/6, -\pi/3, -\pi/3)$, respectively. (g) Energy flow during the braiding process. The three light colored areas indicate the three steps of the braiding process, as discussed in the main text. (a)-(f) correspond to the moments labeled by **I-VI**, respectively. There are always four MZMs (red flat bands at zero energy) and separated by a large energy gap from other modes (blue curves). An animation for the process is provided in the Supplemental Material⁵¹. The dimension of the triangles are $N_x = N_y = 30$, the pairing phases are $\Phi_1 = 0$, $\Phi_2 = -\Phi_3 = 2\pi/3$, and all other parameters are the same as those in Fig. 4.

to be fine tuned.

V. HOLONIMIC GATES

According to the Gottesman-Knill theorem⁵³, the topological quantum gates provided by Majorana braiding are not sufficient for universal quantum computation. The latter requires indeed at least one non-Clifford single-qubit gate, such as the T gate (also known as the magic gate)^{54,55}, which cannot be implemented just by exchanging MZMs⁴⁶. In general, non-topological procedures for realizing a Majorana magic gate require a very precise control of the system parameters and, as a result, they heavily rely on conventional error-correction schemes⁵⁴. In this respect, an interesting role is played by the so-called holonomic gates¹⁹ which, while not being topologically protected, can still feature a good degree of robustness against errors, thus reducing the amount of hardware necessary for subsequent state distillation²⁰.

The minimal model for Majorana-based holonomic gates has been proposed by Karzig *et al.*²⁰ and consists of four "active" MZMs, γ_x , γ_y , γ_z and γ_0 . To successfully implement a holonomic gate, one has to adiabatically vary the three coupling strengths t_i between γ_i (with $i \in \{x, y, z\}$) and γ_0 . Indeed, for every closed loop in the three-dimensional parameter space spanned by (t_x, t_y, t_z) , a difference between the Berry phases picked up by the two states is developed. By properly designing the loop, it is possible to implement a T gate and take advantage of a universal geometrical decoupling in order to suppress the effect of finite control accuracy on the couplings t_i ²⁰. One of the main sources of errors is represented by the parasitic couplings t_{ij} between γ_i and γ_j (with $i, j \in \{x, y, z\}$ and $i \neq j$). These couplings, which are basically unavoidable in a quantum wire-based setup, introduce additional and unwanted dynamical phases, which reduce the gate fidelity (despite error mitigation techniques based on conventional echo schemes)^{20,56}.

Remarkably, SOTS-based setups can naturally guar-

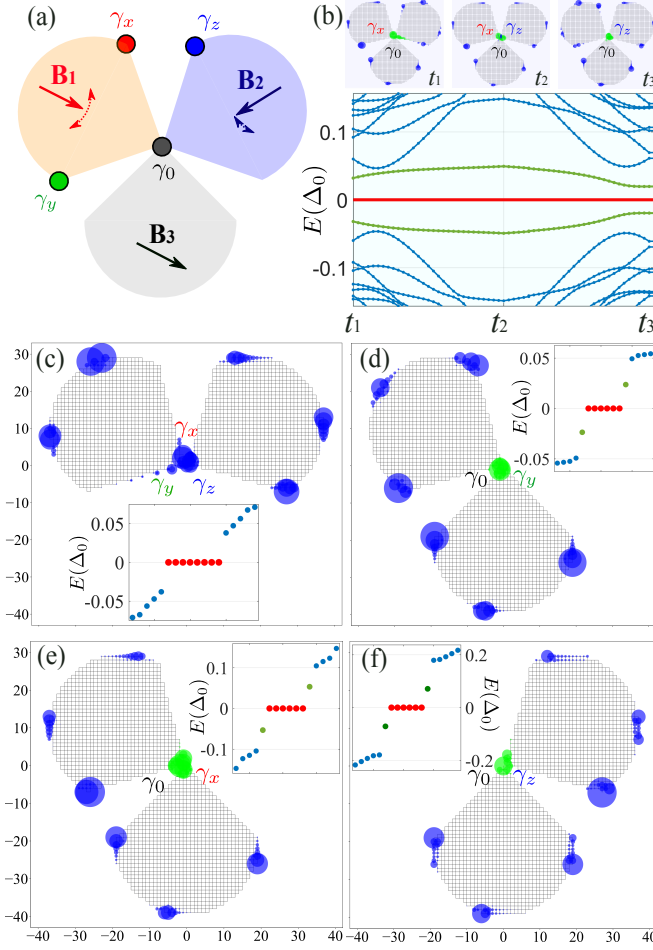


Figure 6. Holonomic gates based on the MZMs. (a) Schematics of the four MZMs γ_x , γ_y , γ_z and γ_0 relevant for the holonomic gates in a shamrock-like trijunction. The positions of these modes are controllable by the magnetic fields \mathbf{B}_1 , \mathbf{B}_2 and \mathbf{B}_3 . (b) Energy flow of the process that first moves γ_z to the center (during $t_1 \rightarrow t_2$) and then moves γ_x away from the center (during $t_2 \rightarrow t_3$). Insets are the positions of MZMs in the initial ($\theta_1 = -\pi/3$ and $\theta_2 = 7\pi/6$), middle ($\theta_1 = -\pi/3$ and $\theta_2 = 4\pi/3$), and final ($\theta_1 = -\pi/6$ and $\theta_2 = 4\pi/3$) states. The green densities are for the fused modes (i.e., two excited modes with lowest energy). (c-f) Coupling between different MZMs, i.e., γ_x and γ_y and γ_z in (c); γ_y and γ_0 in (d); γ_x and γ_0 in (e); and γ_z and γ_0 in (f). The corresponding energy spectra are displayed in the insets. $B_1 = 0.54m_0$ in (a,c-f) and $0.65m_0$ in (a). In (c) $\theta_1 = -\pi/6$, $\theta_2 = 4\pi/3$, (d) $\theta_1 = 0$, (e) $\theta_1 = -\pi/3$, (f) $\theta_2 = 4\pi/3$, for all panels, $\Phi_1 = \Phi_2 = 0$, $\Phi_3 = 2\pi/3$, $B_2 = B_3 = 0.54m_0$, $\theta_3 = -\pi/3$, $\mu = 0$, $\Delta_0 = 0.4m_0$, $m_0 = 2$, $N_r = 20$, while all other parameters are the same as those in Fig. 2.

antee vanishing parasitic couplings, thus providing a novel and convenient platform to study and implement Majorana-based holonomic gates. By exploiting the effective mirror symmetry featured by the SOTs at $\mu = 0$, one can indeed have $t_{ij} = 0$ while still being able to smoothly and freely tune all the other three couplings t_i . In the following, we demonstrate this remarkable feature

with a concrete example.

The setup we propose is a shamrock-like trijunction which is formed by connecting the vertices of three incomplete disks (denoted as S_1 , S_2 and S_3 , respectively) with vanishing μ , as sketched by Fig. 6(a). When the three incomplete disks are disconnected, they each host four MZMs labeled by γ_i with $i \in \{1, 2, 3, 4\}$. The positions of the MZMs are controllable by the applied magnetic fields, as discussed before. For concreteness, we consider the incomplete disks with the same vertex angle of $\pi/2$ and evenly distributed. By properly tuning the magnetic fields \mathbf{B}_1 and \mathbf{B}_2 , i.e., $B_1, B_2 \simeq \sqrt{2}\Delta_0$, $\theta_1 \simeq -\pi/6$ and $\theta_2 \simeq 7\pi/6$, we move the MZMs γ_1 and γ_4 of S_1 and γ_1 of S_2 close to or in the center. Due to the effective mirror symmetry, these three adjacent MZMs cannot interact with each other even if they have strong overlap in their wavefunctions. We thus identify them with γ_x , γ_y and γ_z , respectively. Whether S_1 and S_2 have the same pairing phase or not is not important. We set both at zero $\Phi_1 = \Phi_2 = 0$ for concreteness. On the other hand, we adopt a different pairing phase $\Phi_3 \neq \{0, \pi\}$ in S_3 , and fix the MZM γ_2 or γ_3 of S_3 in the center by tuning \mathbf{B}_3 . This MZM would fuse with γ_i (with $i \in \{x, y, z\}$) if they are brought close to the center. We denote it as γ_0 . The couplings t_i between γ_i and γ_0 are closely determined by their distance. Recalling that these distances are controllable by \mathbf{B}_1 or \mathbf{B}_2 , the couplings are thus smoothly adjustable.

To test our analysis and demonstrate the basic conditions for holonomic gates, we first consider S_1 and S_2 together and move γ_x , γ_y and γ_z all to the center, see Fig. 6(c). From the energy spectrum [the inset of Fig. 6(c)], we find that there is no splitting of MZMs from zero energy. This clearly indicates that γ_x , γ_y and γ_z can never interact with each other. We next consider S_3 together with S_1 or S_2 and move γ_x , γ_y and γ_z to the center, respectively, see Fig. 6(d)-(f). In contrast to Fig. 6(c), evident energy splittings of two original MZMs can be observed (see the green dots in the insets). This signifies the couplings between γ_0 and γ_x , γ_y and γ_z , respectively. The splitting energies are smooth functions of \mathbf{B}_1 or \mathbf{B}_2 . Thus, by tuning \mathbf{B}_1 and \mathbf{B}_2 , we are able to adiabatically adjust the couplings t_i . For illustration, we start with the state, where γ_x and γ_0 are in the center, while the other two not. In this initial state, we have $|t_x| \gg |t_y|, |t_z|$. We slowly move γ_z also into the center by carefully rotating \mathbf{B}_2 and then move γ_x away from the center by rotating \mathbf{B}_1 . In the final state, we arrive at $|t_z| \gg |t_x|, |t_y|$. The instantaneous spectrum for this process is displayed in Fig. 6(b). Two finite energy levels resulting from the coupling of γ_0 and γ_x or γ_z are always present (see the green curves), while the other MZMs stay robust at zero energy. This clearly shows that t_x and t_z are smoothly varied. Similarly, the variation of \mathbf{B}_1 enables us to adjust the other coupling t_y in a smooth manner.

Finally, we note that the shamrock-like trijunction can realize the full parameter space of (t_x, t_y, t_z) . In this sense, a full set of holonomic gates defined by the four

coupled MZMs can be achieved. There are many alternative ways of choosing the four relevant MZMs, which, however, share the essential physics. Other MZMs that exist in the setup but are not relevant to the problem can be safely ignored since they are always far away from the center.

VI. DISCUSSION

There are various candidate systems to implement our schemes. Particularly, the inverted HgTe quantum well in proximity to conventional superconductors and monolayer $\text{FeTe}_{1-x}\text{Se}_x$ have the right properties. The superconducting proximity effect has been realized in HgTe quantum wells^{57,58}. The application of high in-plane magnetic fields is also feasible in experiments⁵⁸. Monolayer $\text{FeTe}_{1-x}\text{Se}_x$ can host a quantum spin Hall phase coexisting with intrinsic superconductivity^{49,59,60}. Importantly, the superconducting gap is comparably large (up to 16.5 meV)⁶¹, and it can sustain a large in-plane magnetic field (up to 45 T)⁶². The localization length of the MZMs can be estimated by $\xi = \max(v/\Delta_0, m/v)$. For typical parameters $v \simeq 1.0 \text{ eV}\cdot\text{\AA}$, $\Delta_0 \simeq 1.0 \text{ meV}$ and $m \simeq 10 \text{ eV}\cdot\text{\AA}^2$, we derive $\xi \simeq 10^3 \text{ \AA}$. Therefore, the length scales for our setups should be larger than 100 nm. For a g-factor close to $g \simeq 2$, a magnetic field of around $\Delta_0/g\mu_B \simeq 10 \text{ T}$ would be sufficient to induce the MZMs.

The MZMs in our setups can be locally probed, for example, by a scanning-tunneling-microscopy tip. Their

existence may be signified as zero-bias peaks in the tunneling conductance⁶³. To read out the qubits in our setups, we may need to convert parity ground states into charge states in isolated islands. In the associated SOTS islands, we can fuse a pair of MZMs by varying the magnetic fields and then perform the parity measurement of the islands, e.g., by applying charge sensors^{64,65}. The parity information encoded in the MZMs could be alternatively measured via the Josephson effect. To do so, we approach an MZM to another one stemming from another island. Then, the Josephson current between the islands can be used to deduce the information⁸.

In summary, we have provided a minimal model for SOTSs and analyzed the MZMs in a disk geometry. We have systematically investigated the fusion of the MZMs. Importantly, we have proposed different setups of SOTSs which allow to implement topological and holonomic gates via braiding and fusion of MZMs. Our results establish SOTSs as an ideal platform for scalable and fault-tolerant quantum information technologies.

VII. ACKNOWLEDGMENTS

We thank Nicolas Bauer, Benedikt Scharf, and Xianxin Wu for valuable discussion. This work was supported by the DFG (SPP1666 and SFB1170 “ToCoTronics”), the Würzburg-Dresden Cluster of Excellence ct.qmat, EXC2147, project-id 39085490, and the Elitenetzwerk Bayern Graduate School on “Topological Insulators”.

* songbo.zhang@physik.uni-wuerzburg.de

† wenbin.rui@gmail.com

¹ Ettore Majorana, Teoria simmetrica dell’elettrone e del positrone, *Nuovo Cimento* **14**, 171–184 (1937).

² A. Y. Kitaev, Unpaired Majorana fermions in quantum wires, *Phys. Usp.* **44**, 131 (2001).

³ J. Alicea, New directions in the pursuit of Majorana fermions in solid state systems, *Rep. Prog. Phys.* **75**, 076501 (2012).

⁴ C. W. J. Beenakker, Search for Majorana Fermions in Superconductors, *Annu. Rev. Condens. Matter Phys.* **4**, 113 (2013).

⁵ S. R. Elliott and M. Franz, Colloquium: Majorana fermions in nuclear, particle, and solid-state physics, *Rev. Mod. Phys.* **87**, 137 (2015).

⁶ N. Read and Dmitry Green, Paired states of fermions in two dimensions with breaking of parity and time-reversal symmetries and the fractional quantum hall effect, *Phys. Rev. B* **61**, 10267–10297 (2000).

⁷ D. A. Ivanov, Non-abelian statistics of half-quantum vortices in p -wave superconductors, *Phys. Rev. Lett.* **86**, 268–271 (2001).

⁸ L. Fu and C. L. Kane, Superconducting Proximity Effect and Majorana Fermions at the Surface of a Topological Insulator, *Phys. Rev. Lett.* **100**, 096407 (2008).

⁹ R. M. Lutchyn, J. D. Sau, and S. Das Sarma, Majorana Fermions and a Topological Phase Transition in Semiconductor-Superconductor Heterostructures, *Phys. Rev. Lett.* **105**, 077001 (2010).

¹⁰ Jay D. Sau, Roman M. Lutchyn, Sumanta Tewari, and S. Das Sarma, Generic New Platform for Topological Quantum Computation Using Semiconductor Heterostructures, *Phys. Rev. Lett.* **104**, 040502 (2010).

¹¹ Y. Oreg, G. Refael, and F. von Oppen, Helical Liquids and Majorana Bound States in Quantum Wires, *Phys. Rev. Lett.* **105**, 177002 (2010).

¹² T.-P. Choy, J. M. Edge, A. R. Akhmerov, and C. W. J. Beenakker, Majorana fermions emerging from magnetic nanoparticles on a superconductor without spin-orbit coupling, *Phys. Rev. B* **84**, 195442 (2011).

¹³ J. Alicea, Majorana fermions in a tunable semiconductor device, *Phys. Rev. B* **81**, 125318 (2010).

¹⁴ S. Nadj-Perge, I. K. Drozdov, B. A. Bernevig, and A. Yazdani, Proposal for realizing Majorana fermions in chains of magnetic atoms on a superconductor, *Phys. Rev. B* **88**, 020407 (2013).

¹⁵ S. Nadj-Perge, I. K. Drozdov, J. Li, H. Chen, S. Jeon, J. Seo, A. H. MacDonald, B. A. Bernevig, and A. Yazdani, Observation of Majorana fermions in ferromagnetic atomic chains on a superconductor, *Science* **346**, 602–607 (2014).

- ¹⁶ A. Y. Kitaev, Fault-tolerant quantum computation by anyons, *Ann. Phys.* **303**, 2–30 (2003).
- ¹⁷ C. Nayak, S. H. Simon, A. Stern, M. Freedman, and S. Das Sarma, Non-Abelian anyons and topological quantum computation, *Rev. Mod. Phys.* **80**, 1083 (2008).
- ¹⁸ S. Das Sarma, M. Freedman, and C. Nayak, Majorana zero modes and topological quantum computation, *npj Quantum Inf.* **1**, 15001 (2015).
- ¹⁹ Paolo Z. and Mario R., Holonomic quantum computation, *Phys. Lett. A* **264**, 94 – 99 (1999).
- ²⁰ T. Karzig, Y. Oreg, G. Refael, and M. H. Freedman, Universal Geometric Path to a Robust Majorana Magic Gate, *Phys. Rev. X* **6**, 031019 (2016).
- ²¹ J. Langbehn, Y. Peng, L. Trifunovic, F. von Oppen, and P. W. Brouwer, Reflection-Symmetric Second-Order Topological Insulators and Superconductors, *Phys. Rev. Lett.* **119**, 246401 (2017).
- ²² Q. Wang, C.-C. Liu, Y.-M. Lu, and F. Zhang, High-Temperature Majorana Corner States, *Phys. Rev. Lett.* **121**, 186801 (2018).
- ²³ Z. Yan, F. Song, and Z. Wang, Majorana Corner Modes in a High-Temperature Platform, *Phys. Rev. Lett.* **121**, 096803 (2018).
- ²⁴ T. Liu, J. J. He, and F. Nori, Majorana corner states in a two-dimensional magnetic topological insulator on a high-temperature superconductor, *Phys. Rev. B* **98**, 245413 (2018).
- ²⁵ M. Geier, L. Trifunovic, M. Hoskam, and P. W. Brouwer, Second-order topological insulators and superconductors with an order-two crystalline symmetry, *Phys. Rev. B* **97**, 205135 (2018).
- ²⁶ C.-H. Hsu, P. Stano, J. Klinovaja, and D. Loss, Majorana Kramers Pairs in Higher-Order Topological Insulators, *Phys. Rev. Lett.* **121**, 196801 (2018).
- ²⁷ Y. Volpez, D. Loss, and J. Klinovaja, Second-Order Topological Superconductivity in π -Junction Rashba Layers, *Phys. Rev. Lett.* **122**, 126402 (2019).
- ²⁸ H. Shapourian, Y. Wang, and S. Ryu, Topological crystalline superconductivity and second-order topological superconductivity in nodal-loop materials, *Phys. Rev. B* **97**, 094508 (2018).
- ²⁹ S.-B. Zhang and B. Trauzettel, Detection of second-order topological superconductors by Josephson junctions, *Phys. Rev. Research* **2**, 012018 (2020).
- ³⁰ S. A. A. Ghorashi, X. Hu, T. L. Hughes, and E. Rossi, Second-order Dirac superconductors and magnetic field induced Majorana hinge modes, *Phys. Rev. B* **100**, 020509 (2019).
- ³¹ R.-X. Zhang, W. S. Cole, X. Wu, and S. Das Sarma, Higher-Order Topology and Nodal Topological Superconductivity in Fe(Se,Te) Heterostructures, *Phys. Rev. Lett.* **123**, 167001 (2019).
- ³² K. Plekhanov, M. Thakurathi, D. Loss, and J. Klinovaja, Floquet second-order topological superconductor driven via ferromagnetic resonance, *Phys. Rev. Research* **1**, 032013 (2019).
- ³³ A. Skurativska, T. Neupert, and M. H. Fischer, Atomic limit and inversion-symmetry indicators for topological superconductors, *Phys. Rev. Research* **2**, 013064 (2020).
- ³⁴ J. Ahn and B.-J. Yang, Higher-Order Topological Superconductivity of Spin-Polarized Fermions, *arXiv:1906.02709*.
- ³⁵ S. Franca, D. V. Efremov, and I. C. Fulga, Phase-tunable second-order topological superconductor, *Phys. Rev. B* **100**, 075415 (2019).
- ³⁶ R.-X. Zhang, W. S. Cole, and S. Das Sarma, Helical Hinge Majorana Modes in Iron-Based Superconductors, *Phys. Rev. Lett.* **122**, 187001 (2019).
- ³⁷ N. Bultinck, B. A. Bernevig, and M. P. Zaletel, Three-dimensional superconductors with hybrid higher-order topology, *Phys. Rev. B* **99**, 125149 (2019).
- ³⁸ Y.-T. Hsu, W. S. Cole, R.-X. Zhang, and J. D. Sau, Inversion-protected higher order topological superconductivity in monolayer WTe₂, *arXiv:1904.06361*.
- ³⁹ Z. Yan, Higher-order topological odd-parity superconductors, *Phys. Rev. Lett.* **123**, 177001 (2019).
- ⁴⁰ X.-H. Pan, K.-J. Yang, L. Chen, G. Xu, C.-X. Liu, and X. Liu, Lattice-Symmetry-Assisted Second-Order Topological Superconductors and Majorana Patterns, *Phys. Rev. Lett.* **123**, 156801 (2019).
- ⁴¹ Y.-J. Wu, J. Hou, Y.-M. Li, X.-W. Luo, and C. Zhang, In-plane Zeeman field induced Majorana corner and hinge modes in an *s*-wave superconductor heterostructure, *arXiv:1905.08896*.
- ⁴² X. Wu, X. Liu, R. Thomale, and C.-X. Liu, High-*T_c* Superconductor Fe(Se,Te) Monolayer: an Intrinsic, Scalable and Electrically-tunable Majorana Platform, *arXiv:1905.10648*.
- ⁴³ X. Zhu, Tunable Majorana corner states in a two-dimensional second-order topological superconductor induced by magnetic fields, *Phys. Rev. B* **97**, 205134 (2018).
- ⁴⁴ M. Ezawa, Braiding of Majorana-like corner states in electric circuits and its non-Hermitian generalization, *Phys. Rev. B* **100**, 045407 (2019).
- ⁴⁵ T. E. Pahomi, M. Sigrist, and A. A. Soluyanov, Braiding Majorana corner modes in a two-layer second-order topological insulator, *arXiv:1904.07822*.
- ⁴⁶ S. Bravyi, Universal quantum computation with the $\nu = 5/2$ fractional quantum Hall state, *Phys. Rev. A* **73**, 042313 (2006).
- ⁴⁷ B. A. Bernevig, T. L. Hughes, and S.-C. Zhang, Quantum Spin Hall Effect and Topological Phase Transition in HgTe Quantum Wells, *Science* **314**, 1757 (2006).
- ⁴⁸ M. V. Durnev and S. A. Tarasenko, Magnetic field effects on edge and bulk states in topological insulators based on HgTe/CdHgTe quantum wells with strong natural interface inversion asymmetry, *Phys. Rev. B* **93**, 075434 (2016).
- ⁴⁹ X. Wu, S. Qin, Y. Liang, H. Fan, and J. Hu, “Topological characters in Fe(Te_{1-x}Se_x) thin films,” *Phys. Rev. B* **93**, 115129 (2016).
- ⁵⁰ E. Khalaf, Higher-order topological insulators and superconductors protected by inversion symmetry, *Phys. Rev. B* **97**, 205136 (2018).
- ⁵¹ See the Supplemental Material for the derivations of boundary states, the wavefunctions and spin polarization of the MZMs, the calculations of fusion strength between the MZMs, and animations for braiding MZMs.
- ⁵² C. W. Groth, M. Wimmer, A. R. Akhmerov, and X. Waintal, Kwant: a software package for quantum transport, *New J. Phys.* **16**, 063065 (2014).
- ⁵³ D. Gottesman, Group22: Proceedings of the xxii international colloquium on group theoretical methods in physics, (1999).
- ⁵⁴ S. Bravyi and A. Kitaev, Universal quantum computation with ideal Clifford gates and noisy ancillas, *Phys. Rev. A* **71**, 022316 (2005).
- ⁵⁵ M. A. Nielsen and I. Chuang, Quantum computation and quantum information, (2002).

- ⁵⁶ T. Karzig, Y. Oreg, G. Refael, and M. H. Freedman, Robust Majorana magic gates via measurements, *Phys. Rev. B* **99**, 144521 (2019).
- ⁵⁷ S. Hart, H. Ren, T. Wagner, P. Leubner, M. Mühlbauer, C. Brüne, H. Buhmann, L. W. Molenkamp, and A. Yacoby, Induced superconductivity in the quantum spin Hall edge, *Nat. Phys.* **10**, 638 (2014).
- ⁵⁸ H. Ren, F. Pientka, S. Hart, A. T. Pierce, M. Kosowsky, L. Lunczer, R. Schlereth, B. Scharf, E. M. Hankiewicz, L. W. Molenkamp, *et al.*, “Topological superconductivity in a phase-controlled Josephson junction,” *Nature* **569**, 93 (2019).
- ⁵⁹ X. Shi, Z.-Q. Han, P. Richard, X.-X. Wu, X.-L. Peng, T. Qian, S.-C. Wang, J.-P. Hu, Y.J. Sun, and H. Ding, FeTe_{1-x}Se_x monolayer films: towards the realization of high-temperature connate topological superconductivity, *Science bulletin* **62**, 503–507 (2017).
- ⁶⁰ X.-L. Peng, Y. Li, X.-X. Wu, H.-B. Deng, X. Shi, W.-H. Fan, M. Li, Y.-B. Huang, T. Qian, P. Richard, J.-P. Hu, S.-H. Pan, H.-Q. Mao, Y.-J. Sun, and H. Ding, Observation of topological transition in high- T_c superconducting monolayer FeTe_{1-x}Se_x films on SrTiO₃(001), *Phys. Rev. B* **100**, 155134 (2019).
- ⁶¹ F. Li, H. Ding, C. Tang, J. Peng, Q. Zhang, W. Zhang, G. Zhou, D. Zhang, Ca.-L. Song, K. He, S. Ji, X. Chen, L. Gu, L. Wang, X.-C. Ma, and Q.-K. Xue, “Interface-enhanced high-temperature superconductivity in single-unit-cell FeTe_{1-x}Se_x films on SrTiO₃,” *Phys. Rev. B* **91**, 220503 (2015).
- ⁶² M. B. Salamon, N. Cornell, M. Jaime, F. F. Balakirev, A. Zakhidov, J. Huang, and H. Wang, “Upper Critical Field and Kondo Effects in Fe(Te_{0.9}Se_{0.1}) Thin Films by Pulsed Field Measurements,” *Sci. Rep.* **6**, 21469 (2016).
- ⁶³ K. Flensberg, Tunneling characteristics of a chain of Majorana bound states, *Phys. Rev. B* **82**, 180516 (2010).
- ⁶⁴ W. G. van der Wiel, S. De Franceschi, J. M. Elzerman, T. Fujisawa, S. Tarucha, and L. P. Kouwenhoven, Electron transport through double quantum dots, *Rev. Mod. Phys.* **75**, 1–22 (2002).
- ⁶⁵ R. Hanson, L. P. Kouwenhoven, J. R. Petta, S. Tarucha, and L. M. K. Vandersypen, Spins in few-electron quantum dots, *Rev. Mod. Phys.* **79**, 1217–1265 (2007).